Commun. Comput. Phys.
doi: 10.4208/cicp.050412.140812a

Vol. **14**, No. 2, pp. 328-354
August 2013

Simulation of Wave-Flow-Cavitation Interaction Using a Compressible Homogenous Flow Method

J. G. Zheng[1], B. C. Khoo[1,2,3,*] and Z. M. Hu[3]

[1] *Department of Mechanical Engineering, National University of Singapore, Singapore 119260.*
[2] *Singapore-MIT Alliance, National University of Singapore, Singapore 117576.*
[3] *Temasek Laboratories, National University of Singapore, Singapore 117411.*

Received 5 April 2012; Accepted (in revised version) 14 August 2012

Available online 27 November 2012

Abstract. A numerical method based on a homogeneous single-phase flow model is presented to simulate the interaction between pressure wave and flow cavitation. To account for compressibility effects of liquid water, cavitating flow is assumed to be compressible and governed by time-dependent Euler equations with proper equation of state (EOS). The isentropic one-fluid formulation is employed to model the cavitation inception and evolution, while pure liquid phase is modeled by Tait equation of state. Because of large stiffness of Tait EOS and great variation of sound speed in flow field, some of conventional compressible gasdynamics solvers are unstable and even not applicable when extended to calculation of flow cavitation. To overcome the difficulties, a Godunov-type, cell-centered finite volume method is generalized to numerically integrate the governing equations on triangular mesh. The boundary is treated specially to ensure stability of the approach. The method proves to be stable, robust, accurate, time-efficient and oscillation-free.

Novel numerical experiments are designed to investigate unsteady dynamics of the cavitating flow impacted by pressure wave, which is of great interest in engineering applications but has not been studied systematically so far. Numerical simulation indicates that cavity over cylinder can be induced to collapse if the object is accelerated suddenly and extremely high pressure pulse results almost instantaneously. This, however, may be avoided by changing the traveling speed smoothly. The accompanying huge pressure increase may damage underwater devices. However, cavity formed at relatively high upstream speed may be less distorted or affected by shock wave and can recover fully from the initial deformation. It is observed that the cavitating flow starting from a higher freestream velocity is more stable and more resilient with respect to perturbation than the flow with lower background speed. These findings may shed some light on how to control cavitation development to avoid possible damage to operating devices.

*Corresponding author. *Email addresses:* mpezhen@nus.edu.sg (J. G. Zheng), mpekbc@nus.edu.sg (B. C. Khoo), huzm@imech.ac.cn (Z. M. Hu)

AMS subject classifications: 35L40, 65M08, 65M22, 76T10

Key words: Cavitating flow, isentropic cavitation model, shock-flow-cavitation interaction.

1 Introduction

Vapour-filled cavities forming in a liquid flow when the pressure drops below the saturated vapour pressure is commonly referred to as cavitation. The cavitation phenomenon is undesired in most situations. An example is that the high pressure pulse and jetting following the collapse of cavitation can damage engineering devices such as propeller, turbomachinery, hydrofoil, etc. On the other hand, attempts also have been made to utilize cavitation effects to improve the performance of engineering machines. For example, the drag exerted on an underwater projectile can be reduced significantly by a supercavitating vapour enveloping the whole object, since the viscous drag is normally about 1000 times less in vapour than in liquid water. During the past few decades, investigation of cavitation has received increasing attention.

Numerically simulating cavitating flow is challenging in terms of modeling of complex physics in the interfacial region separating liquid and vapour phases as well as development of robust numerical methods. Up to now, quite a few numerical approaches have been developed to resolve the cavitating problems and can roughly be categorized into two families. One of them is the so-called sharp interface method where the interface separating the cavitation region and liquid flow is assumed to be a sharp discontinuity and tracked accurately using an iterative procedure, see [5,6] for a brief discussion. Unfortunately, the sharp interface method appears to be able to handle simple cavitating problems only. The other is the widely used diffuse interface method. Instead of attempting to locate the phase interface accurately, the method allows the flow to transmit from vapour to liquid phase smoothly, leading to a numerically diffused zone along the cavitation boundary. The diffuse interface method is becoming increasingly popular because it is simpler than the sharp interface method and can still model some physical details of the cavitating flows accurately. In practical implementation, one has two choices of governing equations, i.e. single-phase or two-phase formulation, on which the complexity of the diffuse interface method depends. For the strict two-phase model, both phases coexist at every point in the flow field and thus one has to solve the separate governing equations for each phase. The complex physics on the interfacial region such as heat and mass transfer, surface tension and restoration of pressure equilibrium between different phases can be taken into account in this type of model. But the governing equations usually involve transfer terms accounting for phase transition and interaction and may not be conservative, and therefore it is not trivial to efficiently solve them. Another disadvantage of the two-phase formulation is that it is difficult to know the parameters associated with phase transition a priori. On the contrary, one-phase model treats the cavitating flow as a single-fluid flow of the mixture of liquid and vapour phases. The flow is gov-

erned by one set of partial differential equations. The model is based on the assumption of kinematic and thermodynamic equilibrium. A major issue is to provide an appropriate equation of state (EOS) to close the model. The physical phenomena of interest including phase transition, dynamic evolution of cavitation and shock wave propagation can be modeled successfully with the one-fluid formulation. However, the non-equilibrium effects cannot be modeled as vapourization and condensation processes are assumed to complete instantaneously. The one-fluid model has been widely used for its simplicity. One can refer to [2,3,7,21–23] for a brief review of the cavitating flow study.

Although much literature is available on the simulation of cavitating flow as well as on analysis of various cavitating features like the inception, evolution, unsteadiness and stability of cavitation, few works exist on the study of such cavitation subjected to external perturbations such as the variation of freestream flow speed or pressure like impact of shock wave or other complex waves. In particular, our interest is focused on the supercavitating underwater object traveling at high speed and exposed to a nearby underwater explosion and the study of the associated dynamics of the cavitating flow impacted by underwater shock wave. In this paper, the cavitating flow interacting with such a wave is investigated systemically under varying freestream flow speed and shock Mach number. The influence of shock strength and upstream flow speed on the development and evolution of cavitation is examined carefully. The unsteady process of supercavity formation, growth, evolution and even collapse is reproduced through our numerical experiments and findings on dynamics of cavitation are reported. Hopefully, this study will enhance our understanding of physics of perturbed cavity and further help us find potential way to minimize negative effects of cavity collapse.

On the other hand, to resolve the pressure wave-cavitation interaction, a numerical method is presented based on a one-fluid homogeneous model. The isentropic EOS for cavitation region [2] together with Tait EOS for water is used to complete the model system. However, correctly and efficiently solving the governing equations is proved to be challenging. It is found that some of the classical schemes for hyperbolic systems of conservation laws cannot be applied directly to the current physical model due to large stiffness of Tait EOS and enormous difference in speed of sound between liquid and vapour phases. Here, MUSCL scheme [10,25] is extended to integrate the system of equations on unstructured triangular mesh which is employed to discretize potentially complex computational domain. A key step in solution procedure is to treat boundary via the use of ghost cells to ensure code stability. The present method exhibits several advantages over some of other approaches. First, the one-fluid homogeneous system employed here is quite simple relative to multi-phase models. But the unsteady cavitating flow features can be modeled properly. Second, the method is quite stable and robust. At high Courant-Friedrichs-Lewy (CFL) number, the method converges rapidly. Third, the phase interface separating liquid water and vapour is resolved sharply and free of non-physical pressure oscillations, even though the CFL number is set as high as 0.8. The paper is organized as follows. In Section 2, the governing equations together with closure conditions are presented. The numerical procedure to solve the model system is

detailed in Section 3. The method is validated in Section 4. In Section 5, the numerical results on pressure wave-cavitation interaction are presented and discussed. Finally, a brief summary is given in Section 6.

2 Governing equations

In this study, a homogeneous model is employed where the liquid and vapour phases are assumed to be in kinematic and thermodynamic equilibrium, that is, liquid and vapour contained in a fluid element share the same velocity, pressure and temperature. The motion of mixture of two phases behaving as one single component is governed by time-dependent Euler equations,

$$\frac{\partial U}{\partial t}+\frac{\partial F}{\partial x}+\frac{\partial G}{\partial y}=-\frac{i}{y}S, \tag{2.1}$$

where i takes value of 0 and 1 for planar and axisymmetric flows, respectively. Here, U, F, G and S are the vector of conserved variables, inviscid flux vectors in x and y directions, geometric source term vector associated with axisymmetric flow, respectively, and are given by,

$$U=\begin{pmatrix}\rho\\ \rho u\\ \rho v\end{pmatrix},\quad F=\begin{pmatrix}\rho u\\ \rho u^2+p\\ \rho uv\end{pmatrix},\quad G=\begin{pmatrix}\rho v\\ \rho uv\\ \rho v^2+p\end{pmatrix},\quad S=\begin{pmatrix}\rho v\\ \rho uv\\ \rho v^2\end{pmatrix}, \tag{2.2}$$

with ρ being the averaged density, u the averaged x velocity component, v the averaged y velocity component and p the averaged pressure. Energy equation is decoupled from model system (2.1) as the flow is assumed to be isentropic, i.e. the pressure is the function of density only.

Obviously, a closure condition in the form of equation of state (EOS) has to be provided to complete system (2.1). For liquid water, Tait equation of state is widely used in many applications and hence employed in this study. A key issue in the cavitating flow simulation is to develop an appropriate EOS to model the thermodynamic behaviors of the liquid-vapour mixture in the cavitation region. Up to now, much effort has been made and various formulations have been proposed. Perhaps, the easiest way is to fix the pressure at a prescribed value once the density drops below a threshold value and this results in the so-called cut-off model,

$$p=\begin{cases}B\left(\dfrac{\rho}{\rho_0}\right)^N-B+A, & \rho\geq\rho_{sw},\\ p_{sat}, & \rho<\rho_{sw},\end{cases} \tag{2.3}$$

where N, A, B, ρ_0 are the material-dependent constants of Tait EOS. For pure liquid water, they are set to be $N=7.15$, $A=10^5$Pa, $B=3.31\times10^9$Pa, $\rho_0=1000kg/m^3$, respectively. Here,

ρ_{sw} is the saturated water density corresponding to saturated vapour pressure p_{sat}. In the pure liquid water region, the pressure is related to the density through Tait EOS, while in the cavitation region, the pressure is fixed at p_{sat}. Although this model can be implemented easily, it has some limitations: the conservation of some flow quantities may not be maintained and the hyperbolic system of equations (2.1) may degenerate non-physically due to zero speed of sound.

To overcome the shortcomings of cut-off model, a mathematically more consistent, isentropic one-fluid formulation was proposed with the assumption that the cavitating flow is the homogeneous mixture of isentropic vapour and liquid [2]. This isentropic model is given by,

$$\rho=\begin{cases}\rho_0\left(\dfrac{p+B-A}{B}\right)^{1/N}, & p\geq p_{sat},\\ \dfrac{k\rho_g^{cav}+\rho_l^{cav}}{\left(\frac{p+B-A}{p_{cav}+B-A}\right)^{-1/N}+k\left(\frac{p}{p_{sat}}\right)^{-1/\gamma}}, & p<p_{sat},\end{cases} \tag{2.4}$$

where $k=\alpha_0/(1-\alpha_0)$ and α_0 is the known void fraction of the mixture density at p_{sat}. Here, ρ_g^{cav} and ρ_l^{cav} are the associated vapour and liquid densities at the cavitation pressure p_{sat}. The adopted assumption that the cavitating flow is the homogeneous and barotropic mixture of vapour and liquid leads to a theoretical expression for sound speed [1,24],

$$a=\left\{\rho\left[\frac{\alpha}{\rho_{sv}a_v^2}+\frac{1-\alpha}{\rho_{sw}a_w^2}\right]\right\}^{-\frac{1}{2}}, \tag{2.5}$$

where a_v and a_w are the speeds of sound of vapour and liquid at a given pressure, respectively. The averaged density of the mixture, ρ, is defined as the linear combination of the saturated vapour and water densities,

$$\rho=\alpha\rho_{sv}+(1-\alpha)\rho_{sw}. \tag{2.6}$$

The isentropic model is consistent with the sound speed formulation adopted and therefore is mathematically sound and physically reasonable [2]. It can strictly guarantee the hyperbolicity of model system (2.1) and does not constraint the ratio of liquid to vapour density. One disadvantage of the model is that one has to solve for the pressure using a fairly time-consuming iterative procedure. In the present study, all the simulations below are based on the isentropic cavitation model.

The present study is concentrated on the simulation of unsteady cavitating flow involving dynamic appearance, evolution and collapse of cavitation and on cavitation dimension as well as pressure pulse due to its collapse. The homogeneous model (2.1) together with isentropic cavitation formulation (2.4) is able to model the macroscopic phenomena stated above and therefore is adopted here. In model system (2.1), effects of viscosity, turbulence, thermal non-equilibrium, surface tension, etc are considered to

be less important and are ignored. Phase transition, which is one of the most important physical processes, can be modeled by one-fluid system (2.1) and is assumed to complete instantaneously. In other words, during phase change, the vapour and liquid phases in the mixture reach mechanical and thermodynamic equilibrium at infinite speed. Hence, detailed physics related to phase change and non-equilibrium effects cannot be resolved by (2.1). These complex physics and effects can be taken into account in multi-phase models such as those of Kunz et at. [27] and of Saurel et al. [26]. The multi-phase models are more physically reasonable. However, one has to determine a number of empirical parameters associated with phase exchange rate, viscous frication, etc. In addition, numerically discretizing the governing equations for multi-phase flow may not be easy. The sound speed expression (2.5) is validated against experimental data in [24] and found to be sound and accurate for mixture in thermodynamic equilibrium with effect of mass transfer on sound speed ignored [2, 24].

3 Numerical method

The homogeneous model (2.1) appears quite simple. But efficiently solving it can be very challenging. A difficulty encountered in calculation is that in liquid phase modeled by Tait EOS, the pressure is highly sensitive to small change in the density. In Fig. 1(a), the pressure is plotted against the density for Tait EOS and isentropic cavitation model in logarithmic scale. The part of pressure-density curve corresponding to Tait EOS is almost vertical, as illustrated in Fig. 1(a). When the pressure drops from 1 amt (10^5Pa) marked as square in Fig. 1(a) to saturated vapour pressure of $p_{sat} = 62.5$ Pa shown as circle, the corresponding density variation is around $0.042 kg/m^3$ which is extremely small relative to water density of $1000 kg/m^3$ at atmospheric pressure. This means that any small change in the density can results in huge pressure jump. As a result, the cavitating flow is sensitive to small perturbation and numerical code may be very unstable. Another problem in simulation is that the local flow Mach number varies dramatically as sound speed may be several orders of magnitude smaller in cavity than in water as shown in Fig. 1(b) where the sound speed model (2.5) of Wallis [24] is depicted. The liquid phase is almost incompressible at a relatively large cavitation number. In addition, spurious pressure oscillations may occur on cavity boundary due to difference in equations of state between cavitation region and liquid phase. As a result of the abovementioned problems, some of conventional compressible flow solvers do not perform well or fail when applied directly to simulation of cavitation. For instance, some high-order schemes appear more diffusive in resolving the cavitating flow, resulting in a more smeared vapour-water interface, and are stable only at relatively small CFL number. With increasing CFL number, the codes based on these methods may crash or produce pressure oscillations across the cavity interface. In this study, the classical MUSCL scheme is employed to discretize the convective terms of system (2.1) as this scheme is known for its stability and robustness. The time-marching is handled using the second-order Runge-Kutta method while the source

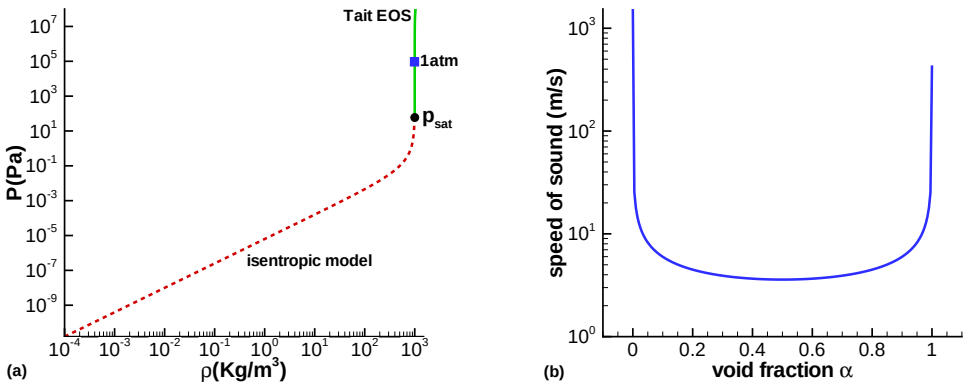

Figure 1: Equations of state and sound speed model: (a) Tait EOS and isentropic cavitation model; (b) speed of sound versus void fraction.

terms are treated separately. Special attention is paid to the treatment of boundary to ensure stability of the code.

3.1 Cell-centered finite volume scheme on triangular mesh

A schematic triangular mesh is shown in Fig. 2. Here, to deal with potentially complex geometry of underwater objects, the computational domain is partitioned into a set of triangles, which is better able to conform to the geometrical features. For the cell-centered approach, the flow variables are defined at the centroid of each triangle, which is the intersection point of three medians of the triangle as illustrated in Fig. 2. Integrating the system of equations (2.1) with source terms ignored over control volume p gives,

$$\frac{\partial U}{\partial t} = -\frac{1}{A}\sum_{k\in Ki(p)}\int (Fn_{pkx}+Gn_{pky})dl, \tag{3.1}$$

where A represents the area of triangle p and $Ki(p)$ denotes the set of indices of three neighboring cells, each of which shares a common edge with triangle p. Here, $\mathbf{n}=$

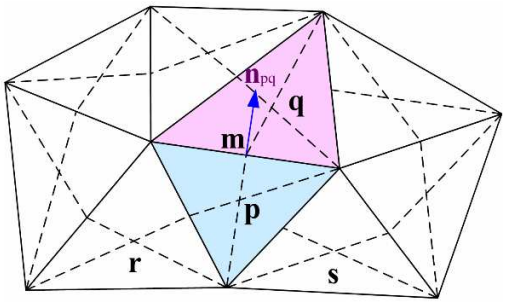

Figure 2: Schematic of control volume definition.

(n_{pkx}, n_{pky}) with $k=r$, s and q is the outward unit vector normal to the common edge of triangles p and k with length l_{pk}. The line integral in Eq. (3.1) can be approximated by using a one-point quadrature rule and assuming the uniform distribution of flux [15,16]. The resulting semi-discrete scheme reads,

$$\frac{\partial U}{\partial t}=-\frac{1}{A}\sum_{k\in Ki(p)}(\tilde{F}n_{pkx}+\tilde{G}n_{pky})l_{pk}, \tag{3.2}$$

where $\tilde{F}$ and $\tilde{G}$ are the numerical fluxes calculated using the HLL Riemann solver as detailed in the next subsection.

3.2 HLL Riemann solver

One way of evaluating the line integral approximation along an edge in Eq. (3.2) is to utilize the rotational invariance property of governing equations (2.1). Eq. (3.2) can be rewritten as,

$$\frac{\partial U}{\partial t}=-\frac{1}{A}\sum_{k\in Ki(p)}T^{-1}\tilde{F}(TU)l_{pk}, \tag{3.3}$$

with the rotation matrix T and its inverse T^{-1} given by,

$$T=\begin{bmatrix}1 & 0 & 0\\ 0 & n_{pkx} & n_{pky}\\ 0 & -n_{pky} & n_{pkx}\end{bmatrix},\qquad T^{-1}=\begin{bmatrix}1 & 0 & 0\\ 0 & n_{pkx} & -n_{pky}\\ 0 & n_{pky} & n_{pkx}\end{bmatrix}. \tag{3.4}$$

By exploiting the rotational invariance property, one can transform the variables in the global coordinate into a local system with x coordinate direction aligned with $\mathbf{n}=(n_{pkx}, n_{pky})$ and y coordinate direction obtained by rotating $\mathbf{n}$ 90 degrees anti-clockwise. In the local coordinate system, a one-dimensional Riemann problem is solved using any accurate or approximate Riemann solvers, and finally the flux is mapped to the global coordinate system. In this study, HLL (Harten, Lax and van Leer) Riemann solver [8] is employed and the numerical flux is calculated as,

$$\tilde{F}^{hll}=\begin{cases}F_L, & \text{if } S_L\geq 0,\\ \dfrac{S_RF_L-S_LF_R+S_LS_R(U_R^{tr}-U_L^{tr})}{S_R-S_L}, & \text{if } S_L<0<S_R,\\ F_R, & \text{if } S_R\leq 0.\end{cases} \tag{3.5}$$

In the above equation, if the left and right states U_L^{tr}, U_R^{tr} for the Riemann problem at mid-point, say $\mathbf{m}$ in Fig. 2, are transformed directly from values U_L, U_R at centroids p and q, respectively, the resulting scheme is first-order accurate only. The left and right wave speeds are given by,

$$S_L=\min(u_L^{tr}-c_L, u_R^{tr}-c_R),\qquad S_R=\max(u_L^{tr}+c_L, u_R^{tr}+c_R), \tag{3.6}$$

with c being the speed of sound. The HLL Riemann solver assumes that the solution is composed of three constant states separated by two waves of speed S_L and S_R.

3.3 Second-order extension in space as well as in time and source terms discretization

The second-order spatial accuracy is achieved through using MUSCL [10, 25]. In this scheme, the flow variables are reconstructed through a linear function rather than the constant distribution employed in Godunov's first-order method. Consider control volume p, the vector of primitive variables $W=(\rho,p,u,v)^T$ on the left hand side of mid-point **m** in Fig. 2 is reconstructed as,

$$W_m^L = W_p + \nabla W_p \cdot \vec{r}_{pm}, \tag{3.7}$$

where W_p is cell averages of the primitive variables defined at centroid p, ∇W_p is the corresponding gradient of W at p, and $\vec{r}_{pm}$ is the distance vector from centroid p to mid-point **m**. Here, the gradient is calculated using least square method which approximates the gradient by fitting values of cell p and those in its neighbors. Next, we apply (3.7) to three neighbors of cell p with $\vec{r}_{pm}$ replaced by the distance vector between two centroids [12, 14],

$$[L_1,\, L_2]\nabla W_p = D, \tag{3.8}$$

where

$$L_1=(\Delta x_{pq},\, \Delta x_{pr},\, \Delta x_{ps})^T, \qquad L_2=(\Delta y_{pq},\, \Delta y_{pr},\, \Delta y_{ps})^T, \tag{3.9a}$$

$$D=(W_q-W_p,\, W_r-W_p,\, W_s-W_p)^T. \tag{3.9b}$$

By applying the least square fitting procedure, the gradient is determined as,

$$\nabla W_p = \frac{1}{l_{11}l_{22}-l_{12}^2}\begin{bmatrix} l_{22}L_1\cdot D - l_{12}L_2\cdot D \\ l_{11}L_2\cdot D - l_{12}L_1\cdot D \end{bmatrix}, \tag{3.10}$$

where $l_{ij}=L_i\cdot L_j^T$. The least square method proves to be more robust and less sensitive to mesh irregularity than Green-Gauss integral formula that is another choice for approximating gradient [12].

In practice, to maintain monotonicity and eliminate oscillations in the flow, a limiter function is usually applied to (3.7) and the limited reconstruction is given by,

$$W_m^L = W_p + \Phi\nabla W_p \cdot \vec{r}_{pm}, \tag{3.11}$$

where Φ is a chosen limiter. Obviously, if $\Phi=0$, formulation (3.11) reduces to the first-order scheme. In the present study, Barth's minmod limiter is employed and defined as [11],

$$\Phi=\min(\Phi_j), \quad j\in Vi(p), \tag{3.12}$$

where $Vi(p)$ is the list of vertexes of cell p and Φ_j is defined as,

$$\Phi_j=\begin{cases}(W_p^{\max}-W_p)/(W_j^r-W_p), & \text{if } W_j^r-W_p>0,\\ (W_p^{\min}-W_p)/(W_j^r-W_p), & \text{if } W_j^r-W_p<0,\\ 1, & \text{if } W_j^r-W_p=0.\end{cases} \tag{3.13}$$

Here, W_j^r is the unlimited reconstruction value at vertex j, and W_p^{min} and W_p^{max} are given by,

$$W_p^{\min}=\min(W_p,\ W_k),\qquad W_p^{\max}=\max(W_p,\ W_k),\qquad k\in Ki(p). \tag{3.14}$$

At this point, the second-order reconstruction procedure is completed and one can construct the flow state on the right hand side of mid-point **m** in the same manner. After the coordinate transformation as detailed in the previous subsection, the Riemann problem is solved and the numerical flux is evaluated. The time discretization is implemented by the second-order TVD Runge-Kutta method developed by Shu and Osher [17]. The semi-discrete form of governing equations, i.e. Eq. (3.2), is replaced with

$$U^{(1)}=U^{(n)}+\Delta tL(U^{(n)}), \tag{3.15a}$$

$$U^{(n+1)}=\frac{1}{2}(U^{(n)}+U^{(1)})+\frac{1}{2\Delta t}L(U^{(1)}), \tag{3.15b}$$

where L is the spatial discretization operator on the right hand side of Eq. (3.2), $U^{(n)}$ is the known conserved variables at time level n and $U^{(n+1)}$ is the solution at new time level $n+1$. The source terms are treated using splitting scheme detailed in [8].

3.4 Boundary conditions

In our numerical experiments, it is found that the treatment of boundary conditions, especially solid boundary, is crucial to ensure stable solution. Various approaches are available for implementing the solid or wall boundary conditions, such as strong formulation where the zero normal velocity across the solid wall is enforced explicitly and weak formulation where the zero normal velocity is enforced in the flux function [13]. Consider triangle I in Fig. 3 which is inside the computational domain with its lower edge located on a physical boundary. In the weak formulation with a vertex-centered finite volume method, one calculates the numerical flux across the boundary directly by substituting the pressure and velocity adopted from interior cells into the physical flux definition. The implementation of the weak boundary conditions is easy and used successfully in gas-dynamics simulation. However, when applied to the solid boundary associated with the current cavitating flow, this strategy gives rise to problems and the resulting method is quite unstable. This may be attributed to the fact that flow variables on the boundary, i.e. the lower edge of cell I, is approximated directly as the corresponding cell averages of cell I. The approximations are less accurate than those based on Riemann solution on edge

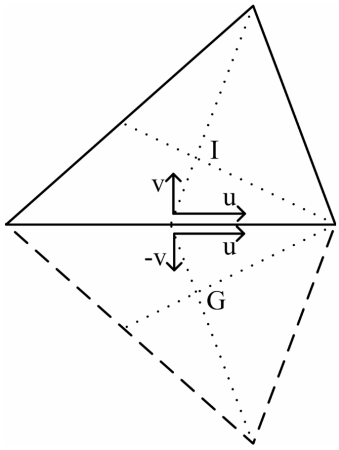

Figure 3: Definition of a ghost cell along a physical boundary.

inside the computational domain. Due to the stiffness of EOS employed, the numerical errors introduced by the approximations on the boundary may be amplified and deteriorate the stability of method. To fix this problem, we resort to the approach of employing ghost cells which are imaginary layers of cells as illustrated in Fig. 3. The approach is similar to those in [9, 13]. In Fig. 3, ghost cell G outside the computational domain and real cell I are symmetric with respect to the edge on the physical boundary. The ghost cells are introduced to simplify the flux calculation on the boundary. The primitive variables in the ghost cells are obtained based on different types of boundary conditions. In the case of solid boundary shown in Fig. 3, the velocity vector in cell G is obtained by reflecting the velocity vector of cell I, while other variables take the values of cell I. With the reconstructed state, the Riemann problem can be solved on the boundary as on an interior edge. The use of ghost cells for treatment of wall boundary is a crucial ingredient of the present method and ensures a robust code.

4 Code validation

In this section, the developed code is validated by resolving some test problems and comparing the numerical results with analytical solution or experimental data. Unless stated otherwise, the isentropic cavitation model is employed with the saturated vapour pressure of 62.5Pa and CFL number is set to 0.8 in all the calculations below.

4.1 Accuracy check with the 1D Riemann problem

To check order of accuracy of our method, we shall consider a single-component problem where the exact solution must be sufficiently smooth. However, for the barotropic flow modeled by system (2.1) together with Tait EOS, it is not possible to find a suitable test

case with smooth solution. Therefore, we have to solve a 1D Riemann problem involving discontinuity. Initially, a $1m$ long tube is filled with two water streams moving in the opposite direction away from the centre of domain with the velocity magnitude of $50m/s$. The pressure is set to 10^8Pa or 1000 atm. The 1D problem is run as a 2D case with y velocity component set to 0 initially. In this case, CFL number is set equal to 0.1 and limiter in (3.11) is turned on in variable reconstruction.

The evolution of initial discontinuity gives rise to a left rarefaction, a right rarefaction and a stationary contact discontinuity in between. There is no cavitation as velocity magnitude is not high enough. The simulation is run to $0.2ms$ on a series of triangular meshes with characteristic grid length of $h_k = 1/N_k$ where $N_k = 40$, 80, 160, 320, 640 and 1280. We calculate L_1 error norm of density, $L_1 = \sum_{i=1}^{N_m} |\rho_i - \rho_{exact}| \Delta\Omega_i$, where ρ_i is the numerical result in cell i, ρ_{exact} is the corresponding exact solution, $\Delta\Omega_i$ is volume of cell i and N_m is the total number of cell elements. The exact solution is obtained using an iterative method as detailed in [8]. Fig. 4 plots L_1 error norm for density shown as solid line with squares against h_k. Although MUSCL is formally a second-order accurate method, the convergence rate for this case is about 1. This is consistent with the facts that the solution contains sharp flow structures and accuracy of MUSCL with limiter locally degrades to first order in the presence of large gradients and local extrema. The method should still be second order accurate over smooth part of the solution.

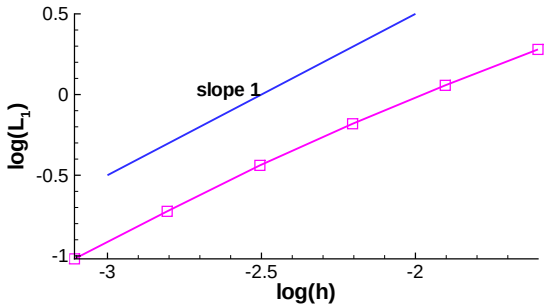

Figure 4: Log-Log plot of L_1 error norm versus h_k for the 1D Riemann problem.

4.2 1D cavitation in an open tube

The second test problem is concerned with a 1D cavitation in a $1m$ long open tube. The initial condition is the same as that of the 1D Riemann problem in Subsection 4.1 except that the velocity magnitude of two water streams is $100m/s$. The initial setup would generate two rarefactions propagating to the left and right, respectively, and a cavitation pocket around the centre of the domain.

An unstructured triangular mesh with $h_k = 1/400m$ is used, as illustrated in Fig. 5. The top and bottom of the computational domain are treated as reflecting boundaries, while the left and right ends are considered as open boundaries. In Fig. 6, the numerical

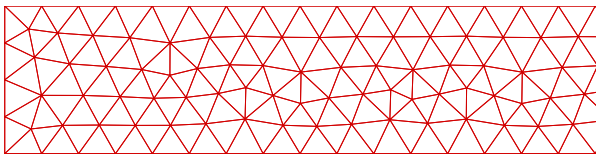

Figure 5: View of the part of triangular mesh used for the 1D cavitating flow.

solution from the isentropic cavitation model at $0.2ms$ is compared with the analytical solution based on Vacuum model developed in [18]. It is obvious that the two solutions are in good agreement. The flow structures including rarefactions and cavitation are well captured. The cavitation boundary is free of pressure oscillations and the code is still stable although CFL number is set at a relatively high value of 0.8. The isentropic model results in the relatively low pressure close to 0 in the cavitation as depicted in the pressure plot of Fig. 6. Our calculation also shows good occurrence with the published results of Liu et al. [2]. The profile of mass fraction of vapour, which is defined as

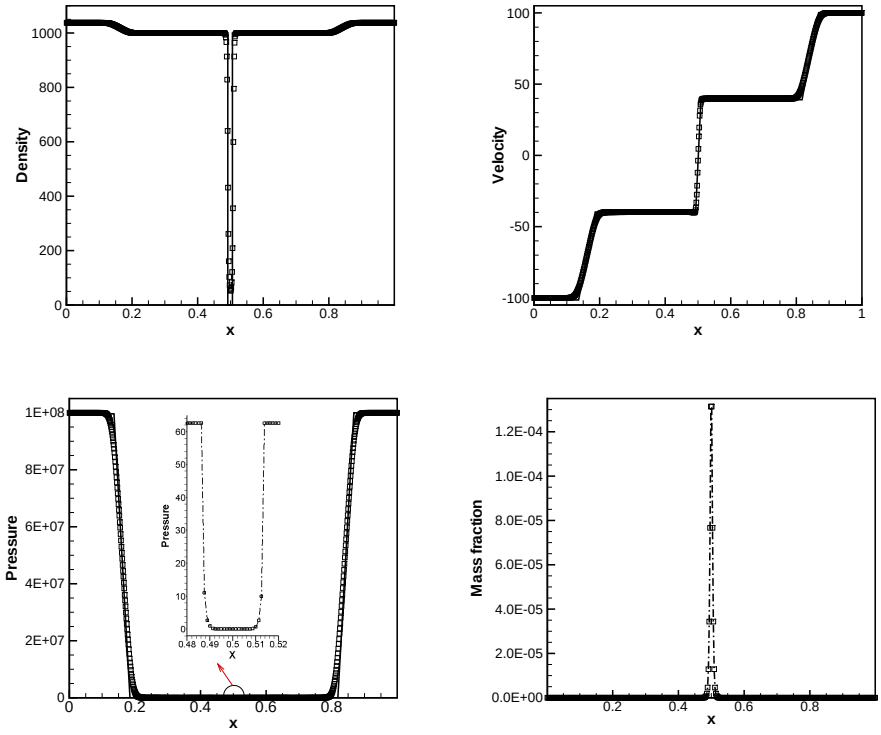

Figure 6: The comparison of numerical solution based on isentropic model (squares) and analytical solution (solid lines) for the 1D cavitating flow at $0.2ms$. The numerical solution is extracted along the centerline of the computational domain shown in Fig. 5. The close-up view of pressure distribution from the isentropic model in the cavitation region is embedded in the pressure plot. The mass fraction profile of vapour is depicted in the last subfigure where the analytical solution is not presented.

$\beta=\alpha\rho_{sv}/(\alpha\rho_{sv}+(1-\alpha)\rho_{sw})$, is presented in the last frame of Fig. 6. The mass fraction is almost 0 outside cavitation. In the cavitation pocket full of the mixture of vapour and water, minimum mixture density is around $50kg/m^3$ and maximum void fraction is greater than 0.9. However, due to the fact that the saturated vapour density is several orders of magnitude smaller than the saturated water density, the mass fraction is quite small in cavitation as shown in Fig. 6. This case indicates that the developed code is able to resolve the 1D cavitating flow correctly.

4.3 Supercavitation over a high-speed underwater projectile

In the third test problem, the experiments of Hrubes [4] for the high-subsonic and transonic conical-shaped underwater projectile are resolved numerically and the modeling results are compared with experimental shadowgraphs. The projectile has a disk cavitator of radius of $0.71mm$, a length of $157.4mm$ and the length to base radius ratio of 24. The experimental water depth is $4m$ and the freestream pressure of approximately 1.4×10^5Pa is used in the simulation. The computational domain is a rectangle with region covering the projectile cut off. A triangular mesh is used with local refinement along the surface of the projectile which is treated as solid boundary. The inflow boundary conditions are imposed on the left hand side of the domain, while the other three sides are treated as open boundaries.

The experimental freestream flow velocity of $970m/s$ results in a small cavitation number of approximately $\sigma=2\times10^{-4}$. The cavitation number representing the surrounding flow conditions is defined as $\sigma=2(p_\infty-p_{sat})/(\rho_\infty U_\infty^2)$, where ρ_∞, p_∞, U_∞ denote the ambient water density, pressure and velocity, respectively; p_{sat} is the saturated vapour pressure set to 62.5Pa. The experimental shadowgraph and numerical density maps in the subsonic regime are compared in Fig. 7. It is clear that the computed flow supercavitation is developed and has enveloped the entire object. It is observed that the experimental supercavity in Fig. 7(a) is qualitatively comparable to the computed cavity shown in Fig. 7(b). The slight asymmetry of the supercavity in the experiment is probably attributed to the projectile that is at a slight angle of attack. In Fig. 8, the computed cavity profiles are compared quantitatively with Hrubes' supercavity size measurements [4] and prediction of Munzer-Richardt theory [20]. The radial coordinate is magnified for clarity. The two numerical cavity profiles are determined at 0.1 and 0.9 void fraction contours, respectively, because the cavity boundary is diffused numerically and no information is given on the overall accuracy bound of the experimental data. As illustrated in Fig. 8, the numerical results are in good agreement with the experimental measurements and the predicted profile by Munzer-Richardt theory, however, is thicker. Our results are also comparable to those published in [3]. In Fig. 7(c), the cavities are compared between the planar and axisymmetric flow configurations. It is found that the cavity size is sensitive to flow regime and is thicker in the planar flow.

The experimental shadowgraph and computed density contour map are presented in Fig. 9 for the projectile traveling at transonic speed corresponding to Mach number

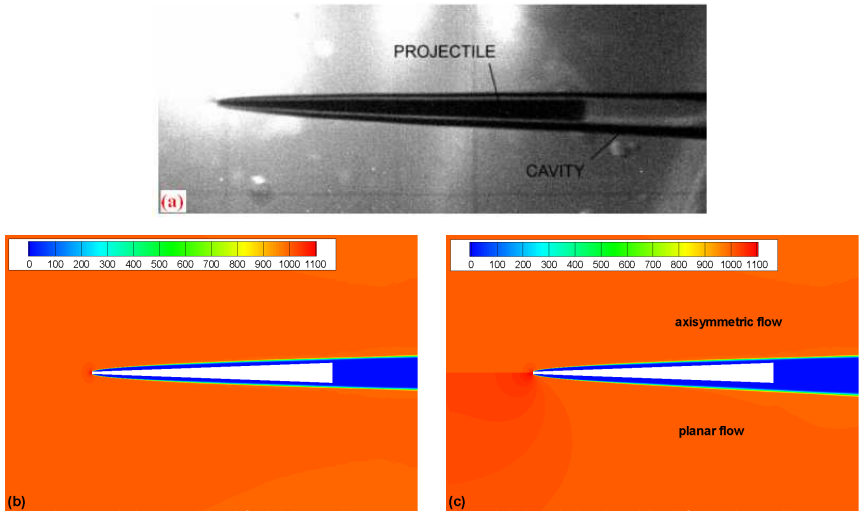

Figure 7: Experimental and numerical results for a high-subsonic underwater projectile at speed of $970m/s$: (a) experimental image of Hrubes [4]; (b) density map with the isentropic cavitation model; (c) comparison between axisymmetric (upper half) and planar (lower half) supercavitation.

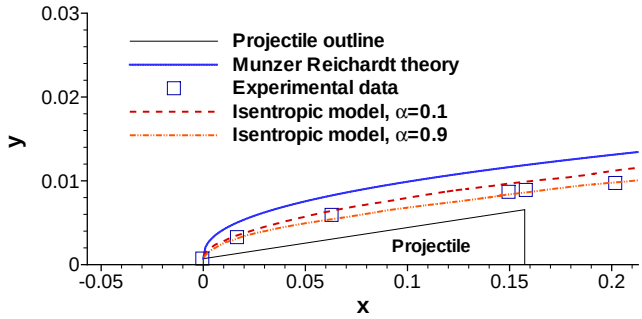

Figure 8: The comparison of supercavity profiles between the theoretical prediction, experimental measurements and numerical simulation for the high-subsonic projectile shown in Fig. 7. The two supercavity boundaries from the numerical results are measured at 0.1 and 0.9 void fraction contours, respectively. Here, the radial coordinate is magnified for clarity.

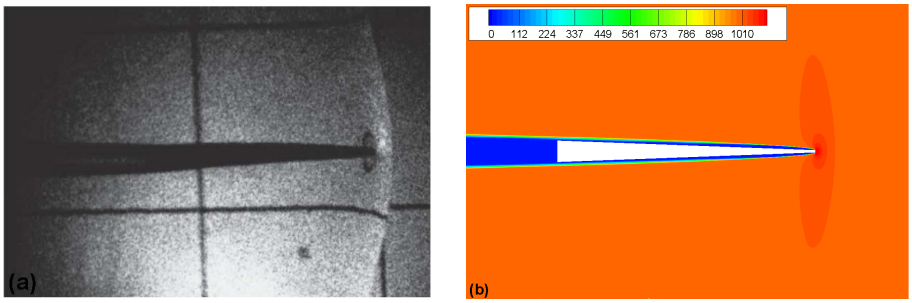

Figure 9: The comparison of the experimental shadowgraph (a) and computed density contour map (b) for the transonic projectile traveling at speed of Mach 1.03.

of 1.03. The numerical setup remains the same except that the object is traveling in the slightly supersonic regime. In the numerical simulation, the detached bow shock in front of cavitator, supercavity and wake are all well resolved. The calculated shock and cavity wake agree well with their counterparts in the experimental shadowgraph. Again, our results are comparable to those presented in [3].

To assess the convergence of the method, the histories of residual errors in the density for the subsonic supercavitating projectile shown in Fig. 7(b) are recorded and plotted in Fig. 10 for CFL numbers of 0.8 and 0.4, respectively. The solution is considered to be convergent only if the residual error drops below 1×10^{-6}. For both CFL numbers, the overall errors are relatively small as the flow field evolves slowly. It is observed that the error corresponding to larger CFL number of 0.8 decreases faster and the convergence criterion is satisfied after approximately 34000 time steps. However, for CFL number 0.4, the solution converges after around 62000 time steps. The computational cost at CFL number 0.4 is about 1.8 times that with CFL number 0.8. It is reported in the literature that some methods are stable only at small CFL value like 0.1. But in the present method, the CFL number is as high as 0.8. Therefore, our method is much more computationally efficient, which is an advantage of our method.

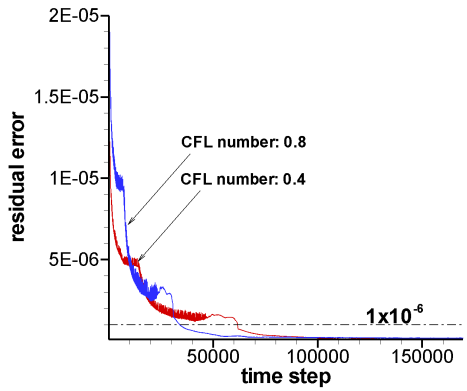

Figure 10: Histories of residual error for the subsonic supercavitating projectile shown in Fig. 7(b).

The 1D and 2D axisymmetric simulations presented here verify the ability of the method to accurately resolve both unsteady and steady cavitations. The numerical results indicate that this method is quite stable, robust and time efficient. It does not produce any pressure oscillations on the cavity boundary at high CFL number and is reliable in simulations.

5 Numerical results and discussion

In this section, the simulation results of pressure wave-cavitation interaction are presented and discussed. Again, the isentropic cavitation model is used and the CFL num-

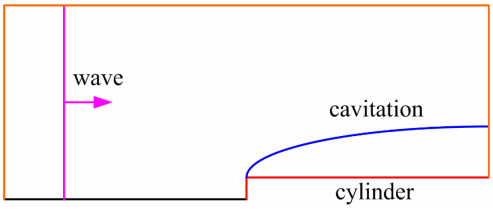

Figure 11: The schematic of computational domain for the cavitation impacted by a wave.

ber is set to 0.8. The axisymmetric supercavitating flow past a cylinder and planar flow around a 2D plane are resolved. The interest is centered on the evolution of the developed cavity as impacted by waves including shock and those arising from freestream velocity change, and the resulting unsteady flow features are examined. The numerical setup for simulations is as follows. The computational domain for each flow configuration is a rectangle $450mm$ long and $300mm$ high. The cylinder immersed in water has the length of $150mm$ and radius of $10mm$. If the object is 2D plane, it is $150mm$ long and $20mm$ high. For object at angle of attack of 0 degree, only the upper half of flow field is resolved due to the symmetry of flow as illustrated in the schematic of numerical setup in Fig. 11. Along the left side of the domain, the flow variables values are fixed as freestream flow conditions, while the top and right sides are treated as open boundaries. The reflecting boundary conditions are enforced along object surface and line of symmetry is treated as symmetric boundary. In all the calculations below, the freestream pressure is initially set to 10^5Pa (1atm).

5.1 On flow supercavitation subjected to freestream velocity increase

A possibly encountered case associated with underwater object is that the object may change its traveling speed along its course. It is therefore of great interest to examine how the cavitation formed over the object responds dynamically to the freestream or inflow velocity variation. The topological change of cavity such as deformation or collapse may affect the performance of the underwater body. Motivated by the abovementioned scenario, a model problem of supercavity subjected to sudden velocity change is considered. Initially, a cylinder with the length of $150mm$ and radius of $10mm$ is submerged in a uniform water flow at the pressure of 10^5Pa and velocity of $100m/s$. Along the inflow boundary on the left side of the computational domain shown in Fig. 11, the freestream pressure and velocity are specified as $p_\infty = 10^5$Pa and $U_\infty = 100m/s$, respectively. With the initial setup, the code is run until a steady state cavity is formed over the cylinder as indicated in Fig. 12(a) where the time coordinate is shifted so that time $t=0$ corresponds to the instant when the supercavity is well developed. Then, from time $t=0$, the incoming freestream speed is changed instantaneously to $120m/s$, while the freestream density and pressure remain unchanged. The cavity evolution process is illustrated through density contour maps in Fig. 12 where $\Delta\tau = 0.1ms$ denotes a fixed time period for ease of compar-

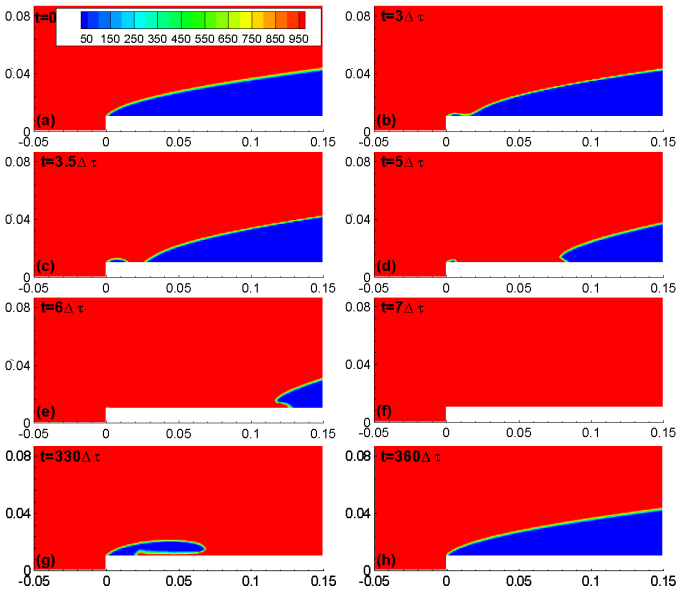

Figure 12: The density contour maps for a supercavity subjected to the sudden freestream velocity increase of $\Delta U = 20m/s$. The initial freestream flow speed is $100m/s$. Here, $\Delta\tau = 0.1ms$.

ison. In Fig. 12(a), the fully developed cavity is shown at $t=0$. The sudden increase in the freestream velocity generates a pressure wave which travels through the computational domain and alters the flow field. The pressure wave is thought to be sufficiently weak and is not reflected visibly in the density plots in Fig. 12. Shortly after the velocity change, the wave has passed over the cylinder head and the leading edge of supercavity has contracted and flattened accordingly as illustrated in Fig. 12(b) at time $t = 3\Delta\tau$. In water at atmospheric pressure, the speed of sound is around $1500m/s$. Hence any perturbation will travel through water very fast and the typical time scale of interest $\Delta\tau$ is fairly small. By $t = 3.5\Delta\tau$, the original supercavity has been cut in half and the two cavities continue to contract as time progresses, see Fig. 12(c). In Fig. 12(d), the dimension of both cavities decreases further and a water jet is formed along the cylinder surface and penetrating into the right cavity. It is also observed that the right or downstream cavity is collapsing from its leading edge while the thickness or vertical extent of the cavity decreases relatively slowly. As time moves on, the upstream or left cavity collapses almost completely and the downstream or right one becomes smaller and smaller as shown in Fig. 12(e) at $t = 6\Delta\tau$. By $t = 7\Delta\tau$, the cavities have vanished, see Fig. 12(f). At this moment, the computational domain is filled with high pressure water. It takes a relatively long time of approximately $350\Delta\tau$ for the pressure to drop below the saturated vapour condition again and for the cavity to appear and eventually envelop the cylinder, see Fig. 12(g)-(h).

The pressure distribution along the cylinder surface is plotted in Fig. 13 at three different times as the cavities are collapsing. At $t=3.5\Delta\tau$, the original supercavity is divided into two cavities as illustrated in Fig. 12(c). In the corresponding pressure plot in Fig. 13,

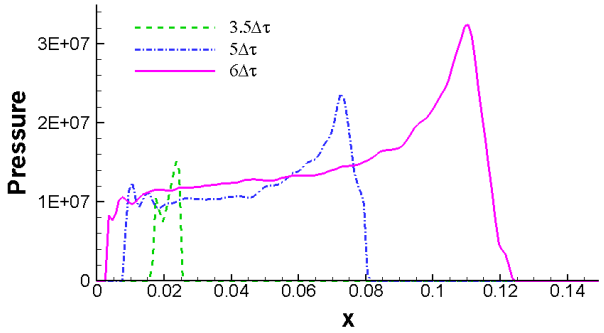

Figure 13: The pressure distribution along the cylinder surface at three different times for the cavitating flow shown in Fig. 12.

the overall pressure has increased dramatically outside the two cavities. There are two local pressure peak values of order of 10^7Pa. One is located immediately behind the trailing edge of the upstream cavity and the other is immediately before the leading edge of the downstream cavity. It is observed that phase transition on the cavities boundaries is followed by the huge pressure pulses which contrast sharply with the pressure values close to 0 before the cavities are destroyed. The pressure pulses then decrease and new pressure extrema appear accompanying further cavities shrinkage. The pressure profile at $t=5\Delta\tau$ in Fig. 13 is similar to that at $t=3.5\Delta\tau$ except that values on the former are larger, especially at the two pressure pulses. At $t=6\Delta\tau$, the upstream cavity almost completely collapses and meanwhile, the downstream cavity becomes smaller and leads to an even larger pressure increase up to 330 atm, see Fig. 12(e) and Fig. 13. The extremely high pressure increase of $\mathcal{O}(100)$ atm caused by the cavities collapse is believed to do serious damage to any underwater devices. Therefore, some protection means is still being explored to avoid the sudden collapse of cavities on the surface of device during change of flow/operating conditions.

The above calculation indicates that the supercavity is highly unstable due to an abrupt increase of 20% in the freestream velocity. Next, the freestream velocity is increased suddenly to $110m/s$ once the steady cavitating flow is reached at $p_\infty=10^5$Pa and U_∞=$100m/s$ and the corresponding supercavity evolution is presented in Fig. 14(a1)-(e1). This flow configuration is similar to the previous one except that the upstream speed is increased by 10% only. The smaller magnitude of freestream velocity jump generates a weaker pressure wave and therefore the supercavity is not destroyed completely by the wave as illustrated in Fig. 14. For the scenario of $\Delta U=20m/s$ as shown in Fig. 12, the original supercavity is split into two cavities which continue contracting and disappear finally. However, this is not the case for the smaller velocity increase magnitude of $10m/s$. By $t=6.5\Delta\tau$, the supercavity has been cut into two parts as illustrated in Fig. 14(b1). The right or downstream cavity contracts from its leading edge and collapses completely with time advancing as shown in Fig. 14(c1)-(d1). But the left or upstream cavity grows and develops into a supercavity enveloping the entire cylinder in a short time of $\mathcal{O}(25)\Delta\tau$, see

Fig. 14(c1)-(e1). The reason that the disturbed flow field by the pressure wave recovers fast to the normal cavitating flow conditions is due to the fact that the pressure wave is much weaker compared with that generated by $\Delta U=20m/s$ and the pressure increase in the flow field following the wave passage is not so high.

Although the magnitude of sudden freestream velocity jump is reduced to $10m/s$, the original supercavity still collapses partially, which is followed by high pressure pulse like that present in the case of $\Delta U=20m/s$. To avoid this, it is suggested the freestream speed be allowed to accelerate uniformly from $100m/s$ to $110m/s$ via $U_\infty=100+at$ where $a=10/(nT)$ is the acceleration, $t\in[0,nT]$ is time and n is an adjustable integer. Beyond time $t=nT$, the freestream velocity is fixed at $110m/s$. Here, the larger n corresponds to a smaller magnitude of constant acceleration and a longer acceleration time. As in [19], the characteristic time T is defined as $T=r_c/a_w$ where r_c is the radius of cylinder and a_w is speed of sound in water at pressure of 1atm. The density contour maps associated with $n=50$, 100 are presented in the second and third columns of Fig. 14, respectively. It is observed that for both accelerations at $n=50$ and 100, the supercavity is not induced to collapse and its boundary is only deformed by the pressure wave arising from the gradual velocity increase. It is also found that the deformation of supercavity boundary resulting from larger acceleration as illustrated in Fig. 14(a2)-(e2) is more severe than the deformation due to smaller acceleration shown in Fig. 14(a3)-(e3). In other words, given a magnitude of freestream speed increase, the smaller acceleration or longer acceleration time results in the slighter deformation. Hence, to avoid the possible cavity collapse and the resulting damage to devices, one can change the velocity of underwater object smoothly.

5.2 On flow supercavitation subjected to freestream velocity perturbation

In practice, the velocity of object may not remain constant and may experience small perturbation or oscillation. This could affect the already existing cavitation over the object. To mimic this process, a sinusoidal perturbation in the freestream velocity is considered. The freestream speed is given by,

$$U_\infty=\begin{cases}100+10\sin\left(\dfrac{2\pi}{nT}t\right), & 0\le t\le nT,\\ 100, & t>nT,\end{cases} \tag{5.1}$$

where t denotes time and nT is the period of perturbation with n being an adjustable integer and T being characteristic time defined in the previous subsection. The initial conditions are the same as those for the sudden velocity increase in the previous subsection. After the supercavity is formed and the flow has reached the steady state, the freestream velocity is changed according to formula (5.1) where time t is measured from this instant. Three sets of density field maps corresponding to $n=5$, 10 and 30, respectively, are presented and compared in Fig. 15. A larger value of n corresponds to a longer period of velocity perturbation and longer response time. Here, only one period of perturbation

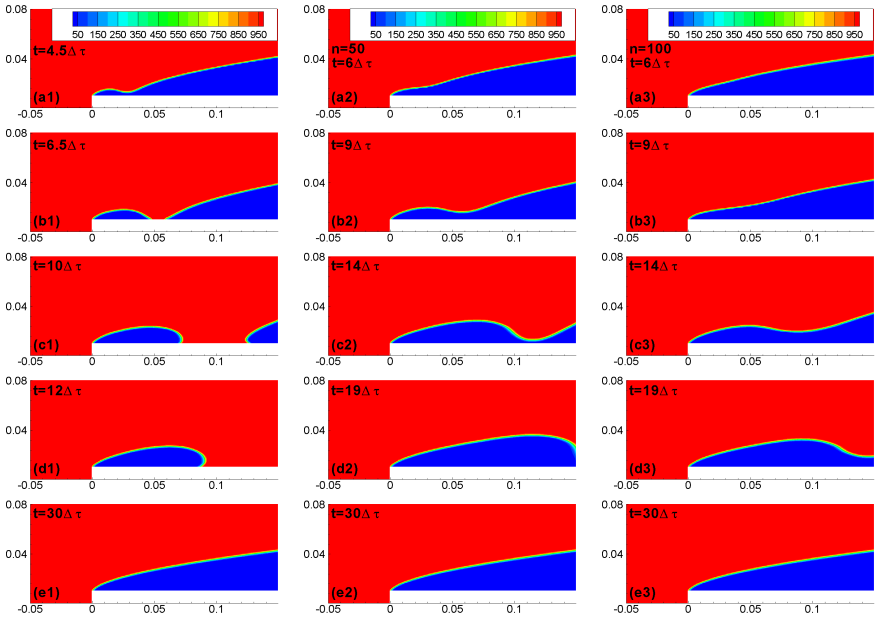

Figure 14: The density contour maps for a supercavity subjected to the freestream velocity change of $\Delta U = 10m/s$. Frames (a1)-(e1): the freestream velocity is increased suddenly from $100m/s$ to $110m/s$; frames (a2)-(e2): the freestream velocity accelerates uniformly from $100m/s$ to $110m/s$, i.e. $U_\infty = 100+at$ with $a = 10/(nT)$, $n = 50$ and $t \in [0, nT]$; frames (a3)-(e3): the uniform acceleration of the freestream speed with $n = 100$. Here, $\Delta\tau = 0.1ms$.

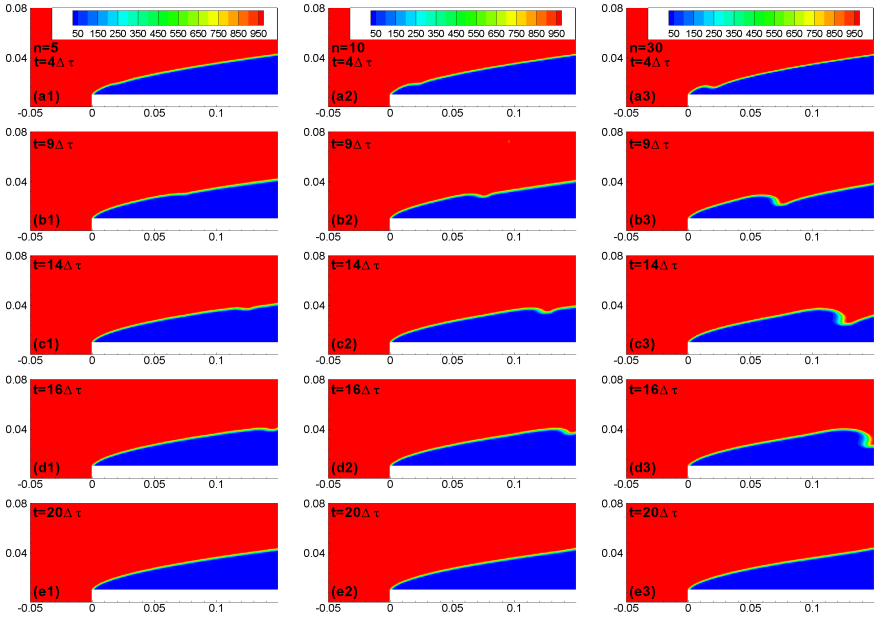

Figure 15: The density field evolution of the cavity with sinusoidal freestream velocity perturbation, i.e. $U_\infty = 100+10sin(2\pi t/(nT))$ with $t \in [0, nT]$. Frames (a1)-(e1): $n = 5$; frames (a2)-(e2): $n = 10$; frames (a3)-(e3): $n = 30$. Here, $\Delta\tau = 0.1ms$.

is implemented with $nT = n \times 6.6\mu s$. This means that in a fairly short time period, the freestream speed reaches the maximum of $110m/s$ first, then decreases to the minimum of $90m/s$ and increases again and finally returns to its original value of $100m/s$. It is observed from the set of density contour maps with $n=5$ (Fig. 15(a1)-(e1)) that a remarkable difference from the sudden velocity change scenario shown in Fig. 14(a1)-(e1) is that the supercavity is only deformed slightly by the pressure wave resulting from the sinusoidal velocity perturbation and does not collapse completely. In Fig. 15(a1) at $t=4\Delta\tau$ with $\Delta\tau=0.1ms$, the freestream speed has recovered to $100m/s$ and the wave has passed over the cylinder. The supercavity boundary is distorted slightly and a ripple is present near the cylinder head. As the freestream velocity is changed smoothly, the generated complex system of wave should be correspondingly weaker than that with the sudden velocity increase. As a result, the supercavity can resist the perturbation and does not lead to total collapse. As time advances, the ripple moves downstream along the cavity boundary, the distorted cavity interface expands transversely and a smooth cavity profile gradually recovers behind the ripple as depicted in Fig. 15(b1)-(d1). After the ripple exits the computational domain, the cavity rapidly recovers to its original shape. In fact, the deformation of supercavity is fairly slight and almost invisible for the case of $n=5$. Next, the period of perturbation is increased by setting n to 10 and 30. The corresponding density evolution processes are illustrated in Fig. 15(a2)-(e2) and (a3)-(e3), respectively. The overall flow patterns for $n=10$ and 30 are similar to that with $n=5$. The supercavity boundary undergoes deformations and eventually recovers to its original shape following wave passage over the whole cylinder. However, the longer the period of perturbation is, the more significant the deformations and ripple are, as demonstrated in Fig. 15. The finding contrasts with the conclusion reached for the flow configuration under the constant acceleration of the freestream speed presented in the previous subsection, where the longer response time or smaller constant acceleration results in the smaller deformation. In the present case, the freestream speed perturbation varies from 0 to a range of values and returns to 0 over the short time period. The deceleration process in the second- and third-quarter of sine perturbation in Eq. (5.1) has the effect of relieving the deformation of the supercavity boundary caused by the pressure wave due to the velocity increase in the first quarter period of sine oscillation. For the smaller period of velocity perturbation, say $n=5$, the velocity increase and decrease processes affect the cavity boundary development in a short time and the combined effect results in the smaller deformation. Here, the freestream velocity perturbation is analogous to a velocity pulse in some sense where its period is relatively small.

5.3 On high-subsonic and transonic supercavitating flow impacted by shock

In this subsection, the simulation of cavitating flow in high-subsonic and transonic regime accelerated by shock wave is performed to examine the influence of freestream flow velocity and shock strength on cavitation development. The initial numerical setup is the same as that employed in Subsection 5.1 except that the freestream velocity is much

higher. The object submerged in water is assumed to be parallel to the flow direction. Again, the calculation for each flow configuration is divided into two steps. After the supercavity is formed, the incident shock wave is introduced along the left hand side of the computational domain by changing the freestream velocity and pressure to the post-shock flow state which is related to pre-shock flow conditions as well as shock Mach number via Rankine-Hugoniot jump relations. The time sequence of computed density contours for the axisymmetric cavitating flow over the cylinder impacted by a Mach 1.1 shock wave are presented in Fig. 16(a1)-(e1), and compared with the corresponding 2D planar cavitating flow depicted in Fig. 16(a2)-(e2). Here, the freestream flow velocity is $1000m/s$, which results in a relatively high traveling speed of perturbation in water. Comparing the two sets of figures, it is observed that the overall flow patterns are similar between the axisymmetric and planar configurations. Take the axisymmetric cavitation as an example of analysis. At $t=13\Delta\tau$ with $\Delta\tau=0.01ms$, the incident shock wave has passed over cylinder head and collided with leading edge of cavitation region. The supercavity appears to be quite stable and is not destroyed by the passing shock wave with its boundary locally taking a saddle shape, see Fig. 16(a1). As demonstrated in Fig. 16(b1), the saddle is observed to be deepening as it moves downstream. At the same time, the cavity interface to the left of the saddle is recovering from the initial deformation. At $t=22\Delta\tau$, the saddle is approaching right end of the computational domain and deepens further; one can refer to Fig. 16(c1). By $t=29\Delta\tau$, it appears that the saddle has cut the supercavity in half and a re-entrant jet like structure is visible near the cylinder end as illustrated in Fig. 16(d1). At $t=59\Delta\tau$, the cavity with smooth profile is recovered. In this case, $\Delta\tau$ is $0.01ms$ and the shock-cavitation interaction process has proceeded very quickly. Recall that the cavity at the freestream velocity of $100m/s$ is destroyed completely by the pressure wave arising from the sudden increase of $\Delta U=20m/s$ in the upstream speed. However, for a Mach 1.1 normal shock propagating through water at atmospheric pressure, the velocity and pressure jumps across the shock are around $\Delta u=76m/s$ and $\Delta p=1.28\times10^8$Pa, respectively. This calculation indicates that the cavity at higher upstream speed is more stable and better able to withstand the imposed perturbation. The evolution process of planar cavity as shown in Fig. 16(a2)-(e2) is similar to the axisymmetric scenario. The major flow feature due to the shock impact is the saddle-like structure traveling along the cavity boundary. But the planar cavity is thicker than the axisymmetric one and is even more resilient and resistant to perturbations, see Fig. 16. The density contours under a higher perturbation at larger Mach 1.2 shock are presented in Fig. 16(a3)-(e3). As perhaps to be expected, the cavity locally collapses with shock strength increasing. The saddle with M=1.2 in Fig. 16(a3) moves a little faster and is deeper compared with that in Fig. 16(a2) at M=1.1, which means that the cavity boundary undergoes a more severe deformation. The increasingly distorted cavity has been cut in half by $t=19\Delta\tau$, shortly after which the right cavity collapses completely while the left one expands downstream as shown Fig. 16(b3)-(c3). By $t=29\Delta\tau$, the left cavity has developed into a supercavity enveloping the object, which simultaneously grows transversely, see Fig. 16(d3)-(e3). Next, the shock Mach number is increased further to 1.6 and

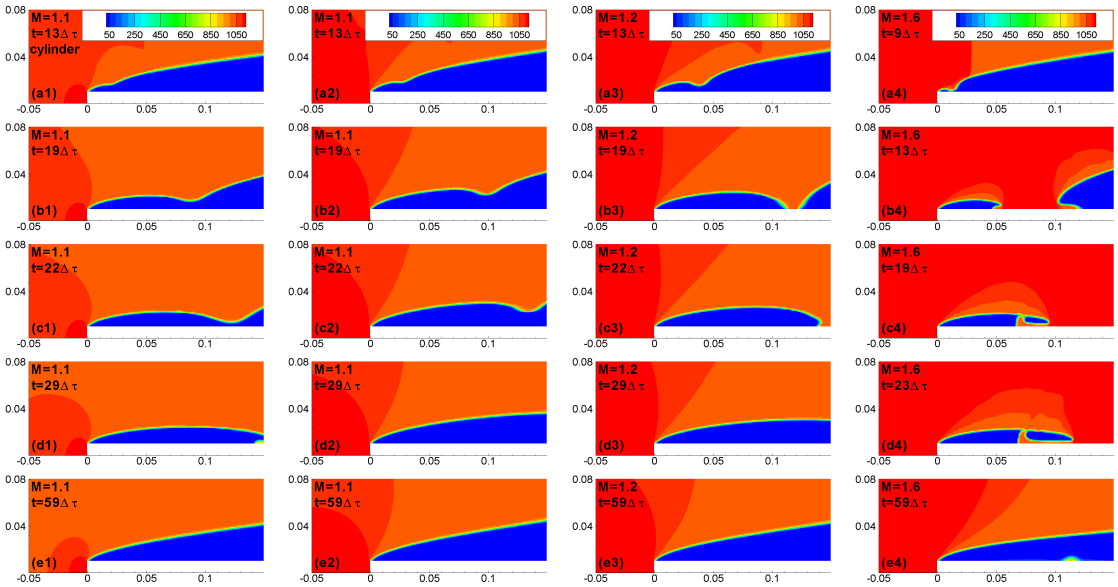

Figure 16: The density contour maps for the cavitating flow impacted by shock. Frames (a1)-(e1): axisymmetric flow; the others: planar flow. Here, $U_\infty = 1000m/s$ and $\Delta\tau = 0.01ms$.

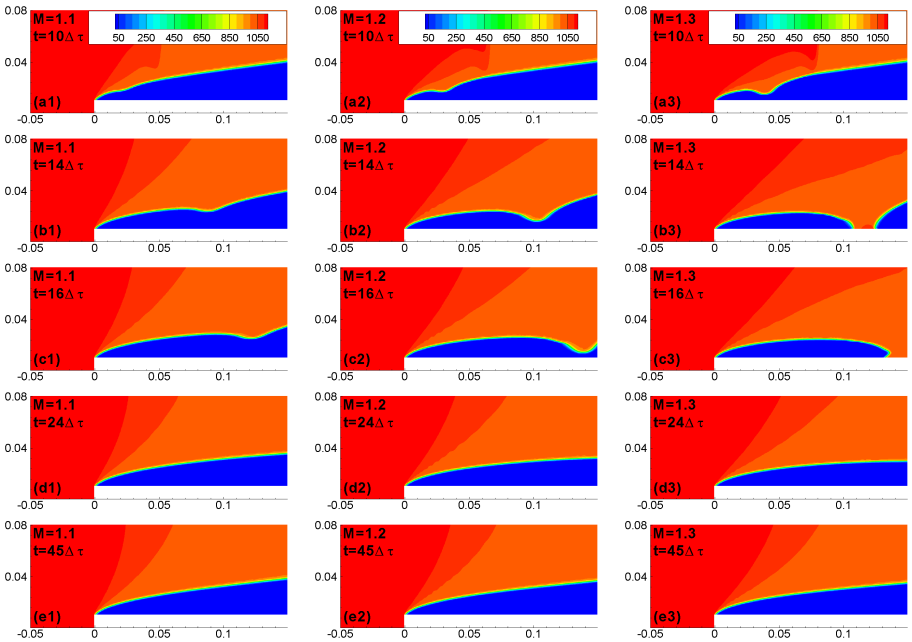

Figure 17: The density contour maps for the planar cavitating flow impacted by shock. Here, $U_\infty = 1500m/s$ and $\Delta\tau = 0.01ms$.

numerical results are presented in Fig. 16(a4)-(e4) where the time sequence is different from that at the lower Mach numbers. The cavity evolution is similar to that with M=1.2, but entails some new flow features. At $t=13\Delta\tau$, a water jet is created from the leading edge of right cavity after the original supercavity is split into two parts. An interesting feature observed is that the left cavity becomes extended while its trailing cavitation region is shed and got convected downstream, see Fig. 16(c4)-(d4). Finally, the upper region cavity continues to grow and envelops the whole object, see Fig. 16(e4).

The planar flow results for higher freestream velocity of $1500m/s$ are illustrated in Fig. 17. For the arrangement with $U_\infty=1500m/s$ and M=1.1, the time evolution of cavity as shown in Fig. 17(a1)-(e1) is fairly similar to that at the lower upstream speed as depicted in Fig. 16(a2)-(e2). As perturbation propagates faster through water at higher freestream speed, the shock-cavitation interaction occurs in a shorter time duration and the cavity evolves faster accordingly, as shown in Fig. 17. The higher upstream speed usually corresponds to a thinner supercavity and therefore the recovered cavity in Fig. 17(e1) is narrower than that in Fig. 16. With $U_\infty=1500m/s$, the supercavity is still stable at M=1.2 and only induced to collapse locally by the higher strength Mach 1.3 shock, see Fig. 17(a2)-(e2) and (a3)-(e3). The calculation shows that the higher the freestream speed is, the more stable the supercavity is. It is also not unexpected that a higher magnitude of perturbation expressed in terms of higher shock strength has led to the collapse of the supercavity.

6 Conclusion

A simple homogeneous flow method is presented for resolving the cavitating flow impacted by the pressure wave. The isentropic cavitation model together with Tait EOS is employed to close the governing equations. Several aspects of the method are outlined. The resulting code is validated against analytical solution and experimental data and proves to be accurate, stable, robust and computationally efficient. Numerical experiments indicate that the treatment of solid boundary through use of ghost cells is key to the stability of the method. The interaction between supercavity and pressure wave is studied systematically for the first time. The sudden acceleration of underwater object may lead to collapse of cavity over it and generate great pressure pulse, which, however, can be avoided by changing the velocity smoothly. The cavity starting from a relatively low freestream speed is usually unstable with respect to the freestream speed variation. On the contrary, for the high-speed flow, although cavity interface may be deformed by the incident shock, well-developed profile can be recovered finally. The larger upstream flow velocity usually leads to the more perturbation resistant cavity. These findings may help us better control the cavitation evolution.

Acknowledgments

The work is supported by ONR (Office of Naval Research) under grant number N000141010474.

References

[1] D. P. Schmidt, C. J. Rutland and M. L. Corradini, A fully compressible two-dimensional model of small high speed cavitating nozzles, Atomization Sprays, 9 (1999), 255-276.

[2] T. G. Liu, B. C. Khoo and W. F. Xie, Isentropic one-fluid modeling of unsteady cavitating flow, J. Comput. Phys., 201 (2004), 80-108.

[3] M. D. Neaves and J. R. Edwards, All-speed time-accurate underwater projectile calculations using a preconditioning algorithm, J. Fluids Eng., 128 (2006), 284-296.

[4] J. D. Hrubes, High-speed imaging of supercavitating underwater projectiles, Exp. Fluids, 30 (2001), 57-64.

[5] E. Goncalves and R. F. Patella, Numerical simulation of cavitating flows with homogenous models, Comput. Fluids, 38 (2009), 1682-1696.

[6] E. Goncalves and R. F. Patella, Numerical study of cavitating flows with thermodynamic effect, Comput. Fluids, (39) 2010, 99-113.

[7] Z. M. Hu, H. S. Dou and B. C. Khoo, On the modified dispersion-controlled dissipative (DCD) scheme for computation of flow supercavitation, Comput. Fluids, 40 (2011), 315-323.

[8] E. F. Toro, Riemann solvers and numerical methods for fluid Dynamics: a practical introduction, Springer-Verlag, Berlin Heidelberg, 1999.

[9] J. Blazek, Computational fluid dynamics: principles and applications, ELSEVIER, 2001.

[10] B. van Leer, Towards the ultimate conservative difference scheme V. A second-order sequel to Godunov's method, J. Comput. Phys., 32 (1979), 101-136.

[11] T. J. Barth and D. C. Jespersen, The design and application of upwind schemes on unstructured meshes, AIAA Report, (1989), 89-0366.

[12] D. J. Mavriplis, Revisiting the least-squares procedures for gradient reconstruction on unstructured meshs, in: Proceedings of the 16th AIAA Computational Fluid Dynamics Conference, Orlando, FL, AIAA Paper, (2003), 2003-3986.

[13] N. Balakrishnan and G. Fernandez, Wall boundary conditions for inviscid compressible flows on unstructured meshes, Int. J. Numer. Methods Fluids, 28 (1998), 1481-1501.

[14] J. S. Park, S. H. Yoon and C. Kim, Multi-dimensional limiting process for hyperbolic conservation laws on unstructured grids, J. Comput. Phys., 229 (2010), 788-812.

[15] I. K. Nikolos and A. I. Delis, An unstructured node-centered finite volume scheme for shallow water flows with wet/dry fronts over complex topography, Comput. Meth. Appl. Mech. Eng., 198 (2009), 3723-3750.

[16] A. I. Delis, I. K. Nikolos and M. Kazolea, Performance and comparison of cell-centered and node-centered unstructured finite volume discretizations for shallow water free surface flows, Arch. Comput. Meth. Eng., 18(1) (2011), 1-62.

[17] C. W. Shu and S. Osher, Efficient implementation of essentially non-oscillatory shock capturing schemes, J. Comput. Phys., 77 (1988), 439-471.

[18] H. S. Tang and D. Huang, A second-order accurate capturing scheme for 1D inviscid flows of gas and water with vacuum zones, J. Comput. Phys., 128 (1996), 301-318.

[19] Z. M. Hu, B. C. Khoo and J. G. Zheng, The simulation of unsteady cavitating flows with external perturbations, submitted for publication in 2011.

[20] R. J. Grady, Hydroballistics design handbook, Vol I, Naval Sea Systems Command, Technical Report No, SEAHAC/79-1, (1979), 38-45.

[21] W. F. Xie, T. G. Liu and B. C. Khoo, Application of a one-fluid model for large scale homogeneous unsteady cavitation: The modified Schmidt model, Comput. Fluids, 35 (2006), 1177-1192.

[22] J. Zhu, T. G. Liu, J. X. Qiu and B. C. Khoo, RKDG methods with WENO limiters for unsteady cavitating flow, Comput. Fluids. 57 (2012), 52-65.
[23] O. C. Delgosha, R. F. Patella, J. L. Reboud, N. Hakimi and C. Hirsch, Numerical simulation of cavitating flow in 2D and 3D inducer geometries, Int. J. Numer. Methods Fluids, 48 (2005),135-167.
[24] G. B. Wallis, One-dimensional two-phase flow, New York: McGill-Hill, 1969.
[25] B. van Leer, Upwind and High-Resolution Methods for Compressible Flow: From Donor Cell to Residual-Distribution Schemes, Commun. Comput. Phys., 1(2) (2006), 192-206.
[26] R. Saurel, F. Petitpas and R. A. Berry, Simple and efficient relaxation methods for interfaces separating compressible fluids, cavitating flows and shocks in multiphase mixtures, J. Comput. Phys., (228) 2009, 1678-1712.
[27] R. F. Kunz, D. A. Boger and D. R. Stinebring, A preconditioned Navier-Stokes method for two-phase flows with application to cavitation prediction, Comput. Fluids, 29 (2000), 849-875.